

# Reconfigurable terahertz metamaterial device with pressure memory

Jinqi Wang,<sup>1</sup> Shuchang Liu,<sup>1</sup> Sivaraman Guruswamy,<sup>2</sup> and Ajay Nahata<sup>1,\*</sup>

<sup>1</sup>Department of Electrical and Computer Engineering, University of Utah, Salt Lake City, Utah 84112, USA

<sup>2</sup>Department of Metallurgical Engineering, University of Utah, Salt Lake City, Utah 84112, USA

\*nahata@ece.utah.edu

**Abstract:** We demonstrate a liquid metal-based reconfigurable terahertz (THz) metamaterial device that is not only pressure driven, but also exhibits pressure memory. The discrete THz response is obtained by injecting eutectic gallium indium (EGaIn) into a microfluidic structure that is fabricated in polydimethylsiloxane (PDMS) using conventional soft lithography techniques. The shape of the injected EGaIn is mechanically stabilized by the formation of a thin oxide surface layer that allows the fluid to maintain its configuration within the microchannels despite its high intrinsic surface energy. Although the viscosity of EGaIn is twice that of water, the formation of the surface oxide layer prevents flow into a microchannel unless a critical pressure is exceeded. Using a structure in which the lateral channel dimensions vary, we progressively increase the applied pressure beyond the relevant critical pressure for each section of the device, enabling switching from one geometry to another (split ring resonator to closed ring resonator to an irregular closed ring resonator). As the geometry changes, the transmission spectrum of the device changes dramatically. When the external applied pressure is removed between device geometry changes, the liquid metal morphology remains unchanged, which can be regarded as a form of pressure memory. Once the device is fully filled with liquid metal, it can be erased through the use of mechanical pressure and exposure to acid vapors.

© 2014 Optical Society of America

**OCIS codes:** (160.3918) Metamaterials; (300.6495) Spectroscopy, terahertz; (160.3900) Metals.

---

## References and links

1. T. J. Yen, W. J. Padilla, N. Fang, D. C. Vier, D. R. Smith, J. B. Pendry, D. N. Basov, and X. Zhang, "Terahertz magnetic response from artificial materials," *Science* **303**(5663), 1494–1496 (2004).
2. H.-T. Chen, J. F. O'Hara, A. K. Azad, A. J. Taylor, R. D. Averitt, D. B. Shrekenhamer, and W. J. Padilla, "Experimental demonstration of frequency-agile terahertz metamaterials," *Nat. Photonics* **2**(5), 295–298 (2008).
3. W. J. Padilla, A. J. Taylor, C. Highstrete, M. Lee, and R. D. Averitt, "Dynamical electric and magnetic metamaterial response at terahertz frequencies," *Phys. Rev. Lett.* **96**(10), 107401 (2006).
4. N. I. Landy, S. Sajuyigbe, J. J. Mock, D. R. Smith, and W. J. Padilla, "Perfect metamaterial absorber," *Phys. Rev. Lett.* **100**(20), 207402 (2008).
5. H.-T. Chen, W. J. Padilla, M. J. Cich, A. K. Azad, R. D. Averitt, and A. J. Taylor, "A metamaterial solid-state terahertz phase modulator," *Nat. Photonics* **3**(3), 148–151 (2009).
6. H.-T. Chen, W. J. Padilla, J. M. O. Zide, A. C. Gossard, A. J. Taylor, and R. D. Averitt, "Active terahertz metamaterial devices," *Nature* **444**(7119), 597–600 (2006).
7. J. Gu, R. Singh, Z. Tian, W. Cao, Q. Xing, M. He, J. W. Zhang, J. Han, H.-T. Chen, and W. Zhang, "Terahertz superconductor metamaterial," *Appl. Phys. Lett.* **97**(7), 071102 (2010).
8. B. Jin, C. Zhang, S. Engelbrecht, A. Pimenov, J. Wu, Q. Xu, C. Cao, J. Chen, W. Xu, L. Kang, and P. Wu, "Low loss and magnetic field-tunable superconducting terahertz metamaterial," *Opt. Express* **18**(16), 17504–17509 (2010).
9. J. N. Koster, "Directional solidification and melting of eutectic GaIn," *Cryst. Res. Technol.* **34**(9), 1129–1140 (1999).
10. M. D. Dickey, R. C. Chiechi, R. J. Larsen, E. A. Weiss, D. A. Weitz, and G. M. Whitesides, "Eutectic gallium-indium (EGaIn): A liquid metal alloy for the formation of stable structures in microchannels at room temperature," *Adv. Funct. Mater.* **18**(7), 1097–1104 (2008).

11. R. C. Chiechi, E. A. Weiss, M. D. Dickey, and G. M. Whitesides, "Eutectic gallium-indium (EGaIn): A moldable liquid metal for electrical characterization of self-assembled monolayers," *Angew. Chem. Int. Ed. Engl.* **47**(1), 142–144 (2008).
12. J.-H. So, J. Thelen, A. Qusba, G. J. Hayes, G. Lazzi, and M. D. Dickey, "Reversibly deformable and mechanically tunable fluidic antennas," *Adv. Funct. Mater.* **19**(22), 3632–3637 (2009).
13. M. Kubo, X. Li, C. Kim, M. Hashimoto, B. J. Wiley, D. Ham, and G. M. Whitesides, "Stretchable microfluidic radiofrequency antennas," *Adv. Mater.* **22**(25), 2749–2752 (2010).
14. J. Wang, S. Liu, Z. V. Vardeny, and A. Nahata, "Liquid metal-based plasmonics," *Opt. Express* **20**(3), 2346–2353 (2012).
15. J. Wang, S. Liu, and A. Nahata, "Reconfigurable plasmonic devices using liquid metals," *Opt. Express* **20**(11), 12119–12126 (2012).
16. S. Zhu, J.-H. So, R. Mays, S. Desai, W. R. Barnes, B. Pourdeyhi, and M. D. Dickey, "Ultrastretchable fibers with metallic conductivity using a liquid metal alloy core," *Adv. Funct. Mater.* **23**(18), 2308–2314 (2013).
17. D. J. Lipomi, B. C.-K. Tee, M. Vosgueritchian, and Z. Bao, "Stretchable organic solar cells," *Adv. Mater.* **23**(15), 1771–1775 (2011).
18. E. Palleau, S. Reece, S. C. Desai, M. E. Smith, and M. D. Dickey, "Self-healing stretchable wires for reconfigurable circuit wiring and 3D microfluidics," *Adv. Mater.* **25**(11), 1589–1592 (2013).
19. M. Rashed Khan, G. J. Hayes, J.-H. So, G. Lazzi, and M. D. Dickey, "A frequency shifting liquid metal antenna with pressure responsiveness," *Appl. Phys. Lett.* **99**(1), 013501 (2011).
20. B. L. Cumby, G. J. Hayes, M. D. Dickey, R. S. Justice, C. E. Tabor, and J. C. Heikenfeld, "Reconfigurable liquid metal circuits by Laplace pressure shaping," *Appl. Phys. Lett.* **101**(17), 174102 (2012).
21. J. C. McDonald, D. C. Duffy, J. R. Anderson, D. T. Chiu, H. Wu, O. J. A. Schueller, and G. M. Whitesides, "Fabrication of microfluidic systems in poly(dimethylsiloxane)," *Electrophoresis* **21**(1), 27–40 (2000).
22. D. Grischkowsky, S. Keiding, M. van Exter, and C. Fattinger, "Far-infrared time-domain spectroscopy with terahertz beams of dielectrics and semiconductors," *J. Opt. Soc. Am. B* **7**(10), 2006–2015 (1990).
23. D. Zrnic and D. S. Swatik, "On the resistivity and surface tension of the eutectic alloy of gallium and indium," *J. Less Common Met.* **18**(1), 67–68 (1969).
24. S. Linden, C. Enkrich, M. Wegener, J. Zhou, T. Koschny, and C. M. Soukoulis, "Magnetic response of metamaterials at 100 terahertz," *Science* **306**(5700), 1351–1353 (2004).
25. D. Roy Chowdhury, R. Singh, J. F. O'Hara, H.-T. Chen, A. J. Taylor, and A. K. Azad, "Dynamically reconfigurable terahertz metamaterial through photo-doped semiconductor," *Appl. Phys. Lett.* **99**(23), 231101 (2011).

## 1. Introduction

Metamaterials have gained significant attention over the last decade because they can exhibit electromagnetic properties that are not readily available in naturally occurring materials [1]. In the terahertz (THz) spectral range, which has traditionally been referred to as the gap in the electromagnetic spectrum, the need for useful device technologies is particularly acute. Nevertheless, a number of device capabilities, including frequency-agile filters [2], switches [3], absorbers [4] and phase modulators [5] have been demonstrated recently. Of particular interest is the ability to tune the resonant response of THz metamaterials, since this can provide for more flexible functionalities. As an example, tuning of the spectral response can be accomplished through the application of optical radiation [3] or an external voltage [6], which can change the carrier density of a semiconductor material that lies within the gap of a split ring resonator. Such changes can also be accomplished through temperature or magnetic control [7, 8], which has been used to switch a superconductor between its normal and superconducting states. However, since all of these implementations are based on the use of solid-state materials, once the devices are fabricated, their basic geometry is fixed. Thus, the basic transmission spectrum is largely unchanged and only the magnitudes of the individual resonances are varied, depending upon the strength of the external excitation.

Since the transmission properties of metamaterials are determined primarily by the geometric parameters of the metallic elements, the functional flexibility of metamaterial devices can improve dramatically if the shape of the metallic element itself can be altered. Liquid metals, such as EGaIn, offer significant benefits for the development of devices in which large-scale reconfigurability is desirable. EGaIn (78.6% Ga and 21.4% In by weight) has many advantageous properties in this regard: i) It exhibits low viscosity in the absence of an oxidized surface. The bulk viscosity is approximately twice that of water [9], ii) it has low toxicity [10], iii) the melting point is  $\sim 15.5^\circ\text{C}$  and is therefore liquid at room temperature, and iv) the EGaIn surface forms a thin passivating oxide layer of gallium, which allows it to support non-spherical shapes [11]. The last two properties make the metal particularly useful

for a variety of stretchable devices, including antennas [12,13], plasmonic devices [14,15], fibers [16], solar cells [17] and 2D and 3D self-healing wires [18]. Furthermore, within the microchannels, the liquid metal only flows when the applied pressure exceeds the critical pressure for that dimension and maintains its structural stability when the applied pressure is relieved [10]. Based on this property, EGaIn has been used to demonstrate pressure-responsive frequency shifting antennas [19] and reconfigurable circuits [20].

In this submission, we demonstrate the utility of EGaIn for metamaterial applications as a pressure driven, pressure memory device. In contrast to earlier demonstrations, the approach described here allows for switching between multiple device configurations, as well as the ability to reset the device. Using well-developed microfluidics technology [21], we use soft lithography techniques to fabricate microfluidic channels that are embedded within a PDMS film. EGaIn is injected into the air voids through injection channels that are common to the individual metamaterial structures. Since the metal elements are based on liquid metals, the device geometry can be easily switched based on the geometry of the microchannels. By reducing the cross-sectional area of specific microchannels, the critical pressure needed to inject EGaIn increases. Thus, by controlling the injection pressure, we can directly control the device geometry and, thus, the spectral properties of the device. This is accomplished by using a device geometry that incorporates three different microchannel cross-sectional areas, which correspond to three different critical pressures. When the applied pressure exceeds each critical pressure, we obtain different device geometries: split ring resonators (SRRs), closed ring resonators (CRRs) and irregular closed rings. The approach is sufficiently general that it can be applied to a wide variety of other geometries and applications.

## 2. Experimental details

We fabricated a device composed of a  $7 \times 9$  array of rings. In the schematic diagram of a unit cell, shown in Fig. 1(a), the lower horizontal channel acted as the common injection channel for all 9 elements in each row, with all 7 injection channels connected via a common inlet reservoir. The outer radius of the rings was  $R_2 = 86 \mu\text{m}$  and the inner radius of the rings was  $R_1 = 68.5 \mu\text{m}$ , corresponding to the first critical channel width of  $W_1 = 17.5 \mu\text{m}$ . The length of the gap in the ring was  $g = 15.5 \mu\text{m}$ , corresponding to the second critical channel width of  $W_2 = 6.2 \mu\text{m}$ . Finally, the third critical channel width,  $W_3 = 4.0 \mu\text{m}$ , was associated with the narrow horizontal section leading to the upper (wider) horizontal channel. Since all of the microchannels were  $10 \mu\text{m}$  in height, only the three critical channel widths determined the operation of the device. The other device parameters included the width of the lower injection channel,  $D_1 = 25.5 \mu\text{m}$ , the width of the upper (diagonal) connection channel,  $D_2 = 18.5 \mu\text{m}$ , the width of top horizontal channel,  $D_3 = 20 \mu\text{m}$ , and the periodicity of rings,  $P = 315 \mu\text{m}$ , along both the x- and y-axes. In Fig. 1(b), we show an optical microscope image of a portion of the ring array, in which EGaIn filled all of the microchannels through the common lower injection channels.

In order to fabricate the device, we first created a template using conventional photolithographic techniques and then transferred the pattern to a PDMS mold. To accomplish this, we coated a silicon wafer with SU-8 3010 photoresist that was spun cast at 5000 rpm for 30 seconds. After soft baking the photoresist at  $95^\circ$  for 2.5 minutes, the wafer was exposed to UV light using a blank mask and then post baked at  $65^\circ$  for 1 minute and then  $95^\circ$  for 1.5 min. The resulting  $6 \mu\text{m}$  thick planar layer was used to improve the adhesion between the silicon wafer and an upper SU-8 patterned layer. This intermediate layer removed the need for additional surface modifications (e.g. through the use of silanes). A second (upper) layer of SU-8 3010 photoresist was then spun cast at 3000 rpm for 30 seconds. After uv exposure of the photoresist using a mask with the appropriate pattern, the wafer was first baked and then developed, yielding a thin  $10 \mu\text{m}$  upper photoresist layer with the designed pattern. This upper layer served as the template for the PDMS structure that was fabricated via soft lithography. A PDMS pre-polymer was mixed with a curing agent using a weight ratio of 7:1, degassed, poured onto the SU-8 template, and cured for 2 hours at  $60^\circ \text{C}$ . After curing, the inverse PDMS replica was peeled off and sealed with a  $120 \mu\text{m}$  thick planar

section of PDMS using a high voltage corona, yielding a 690  $\mu\text{m}$  thick final structure. Finally, the device reservoir was connected to a syringe, which was controlled by a syringe pump through a NanoPort assembly. We also fabricated a flat unstructured 690  $\mu\text{m}$  thick PDMS film to act as a reference in the THz transmission measurements.

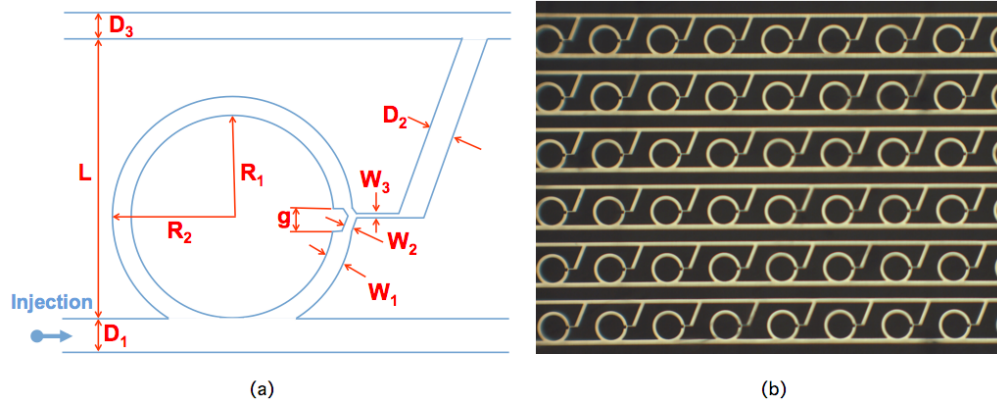


Fig. 1. Schematic diagram of the unit cell. (a) A unit cell from the  $7 \times 9$  array of rings. The device is composed of microfluidic channels fabricated within a PDMS mold. The lower horizontal channel in the figure (width  $D_1$ ) serves as the injection channel for all nine rings in the row. The seven injection channels, one per row, are connected to a common inlet. The periodicity of the rings is  $P = 315 \mu\text{m}$  in both dimensions and the distance between the upper and lower horizontal channels is  $L = 199.5 \mu\text{m}$ . All of the other dimensions are described in the main text. (b) Photograph of the metamaterial device in which all of the microchannels are filled with EGaIn.

We used THz time-domain spectroscopy (THz TDS) to measure the normalized transmission spectra,  $t(\nu)$ , of the electric field through the device, where  $\nu$  is the THz frequency [22]. The sample was mounted on a metal frame in which the opening size exposed only the metamaterial array. Photoconductive devices were used for both emission and coherent detection. An off-axis paraboloidal mirror was used to collect and collimate the THz radiation from the emitter to the device. The THz beam was normally incident on the surface of the metamaterial sample. In contrast to conventional optical measurements, THz TDS allows for direct measurement of the THz electric field, yielding both amplitude and phase information. By transforming the time-domain data to the frequency domain, we are able to determine independently both the magnitude and phase of the amplitude transmission coefficient,  $t(\nu)$ , using the relation

$$t(\nu) = |t(\nu)| \exp[i\phi(\nu)] = \frac{E_{\text{sample}}(\nu)}{E_{\text{reference}}(\nu)}. \quad (1)$$

In this expression,  $E_{\text{sample}}$  and  $E_{\text{reference}}$  are the measured THz electric fields with either the sample or reference in the beam path, respectively, and  $|t(\nu)|$  and  $\phi(\nu)$  are the magnitude and phase of the amplitude transmission coefficient, respectively. While the phase properties of the device are important, we only discuss the amplitude spectra in this work. We measured the injection pressure within the device using a pressure gauge that was connected between the syringe and the inlet through a Y connector. We also numerically simulated the response of the structure. The metal was modeled as a perfect electrical conductor using the device parameters given above, while the dielectric properties of PDMS were taken from THz refractive index measurements [14].

### 3. Results and discussion

In order to demonstrate how the injection pressure can be used to control the transmission properties of this metamaterial device, we slowly ramped the injection pressure applied by the

syringe to a value of  $\sim 255$  kPa. Until that pressure value was reached, there was no EGaIn flow into the main injection channels (width  $D_1$ ). However, when the pressure was further increased above  $\sim 255$  kPa, the main injection channels and split ring channels easily filled with EGaIn. In Fig. 2(a), we show an optical microscope image of a portion of the partially filled array. It is important to note that in all of the unit cells, only the injection channels and SRRs were filled with the liquid metal and there was no leakage into the channels forming the SRR gaps. Importantly, because of the formation of a surface oxide layer that stabilizes the shape of EGaIn, when the injection pressure was released, the device geometry remained unperturbed. This behavior is fundamentally different from that of Hg, which does not form an oxide surface and can retract from the channel when pressure is released because of its high surface energy and lack of a stabilizing mechanism [10].

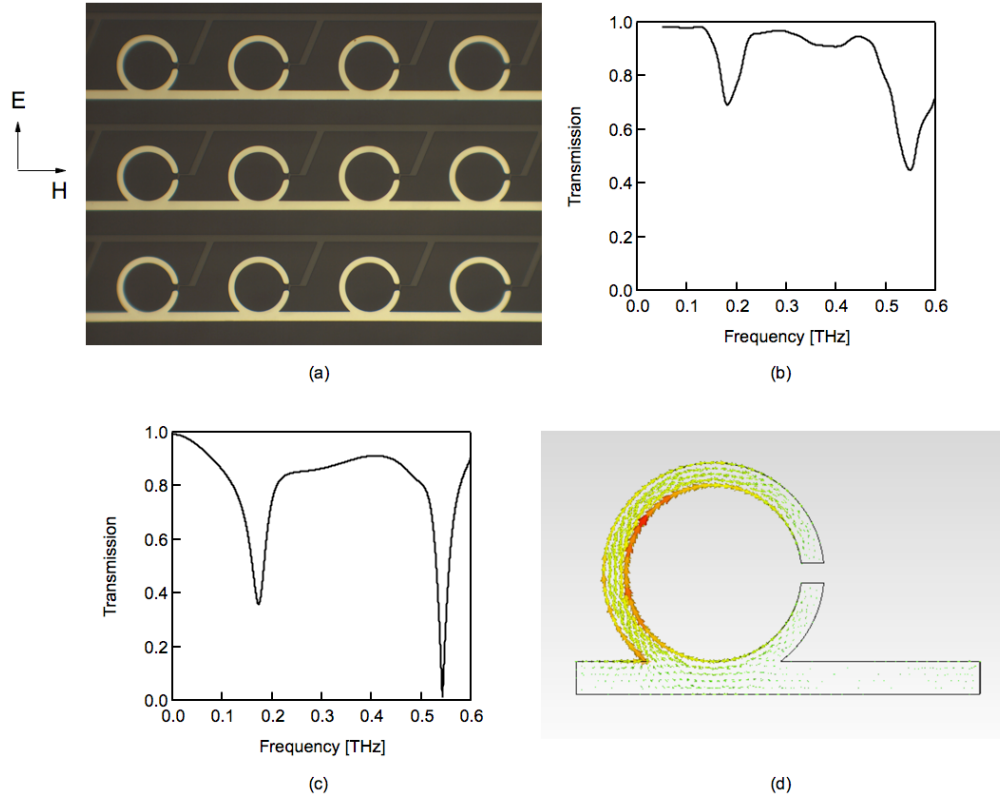


Fig. 2. (a) Photograph of a portion of the split ring resonator array. The background structures in the image are unfilled microchannels. Once the split ring resonators are formed and the pressure is released, this configuration is stable for any applied pressure between 0 and  $\sim 255$  kPa. (b) Measured transmission spectrum with the THz electric field polarized perpendicular to the horizontal injection lines. (c) Numerically simulated transmission spectrum under the same excitation scheme. (d) Snapshot of the numerically simulated current distribution using an excitation frequency of 0.17 THz.

In Fig. 2(b), we show the measured transmission spectrum with the THz electric field normally incident on the device and polarized perpendicular to the injection lines and the gap in the SRRs. In this orientation, the straight injection lines have little effect on the transmitted spectrum. We observe two absorption resonances located at 0.17 THz and 0.54 THz. The center frequencies of these resonances are associated with the orientation of the SRR, its geometrical parameters and the dielectric properties of the surrounding dielectric [3,6]. In Fig. 2(c), we show the numerically simulated transmission spectrum using the same parameters as in the experiments. The resonant frequencies found here are the same as in the experimental results, although the latter resonances are shallower. We attribute the difference

between these spectra primarily to the fact that periodic boundary conditions were used in the numerical simulations, while a finite array was used in the experiments. Furthermore, the metal was modeled as a perfect electrical conductor in the simulations, while EGaIn has a DC conductivity that is more than an order of magnitude smaller than that of Au [23]. Finally, although soft lithography techniques allow for the fabrication of relatively high precision samples, the application of an injection pressure may lead to small differences between individual unit cells, especially in the length of the SRR gaps.

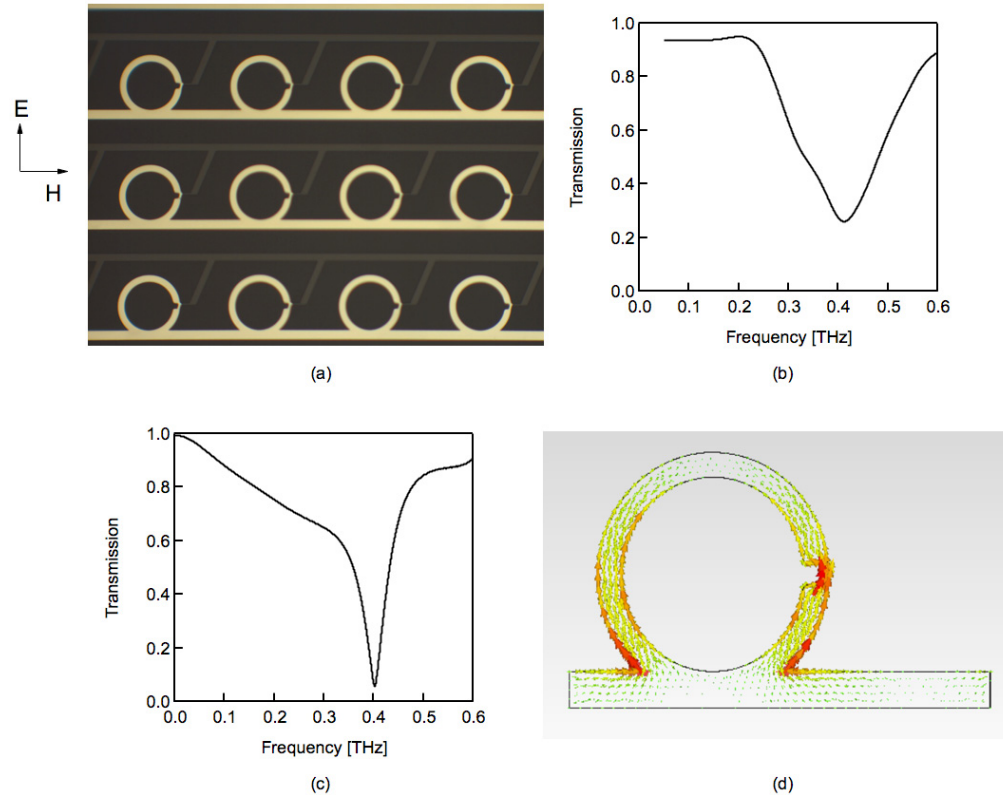


Fig. 3. (a) Photograph of a portion of the closed ring resonator array. The background structures in the image are unfilled microchannels. Once the CRRs are formed and the pressure is released, this configuration is stable for any applied pressure between 0 and  $\sim 296$  kPa. (b) Measured transmission spectrum with the THz electric field polarized perpendicular to the horizontal injection lines. (c) Numerically simulated transmission spectrum under the same excitation scheme. (d) Snapshot of the numerically simulated current distribution using an excitation frequency of 0.40 THz.

The origin of the resonances in SRRs is well known at this point. The absorption resonance at 0.17 THz arises from an LC response of the SRR, in which circulating currents produced from the incident time varying electric field generates a magnetic field polarized perpendicular to the plane of device. In Fig. 2(d), we show a snapshot of the current distribution using an excitation frequency of 0.17 THz, which clearly shows the circulating current. The resonance at 0.54 THz is associated with a higher order dipole resonance, which arises from currents induced by the electric field of the incident radiation on opposite sides of the SRRs. This resonance is related to the plasmon resonance of cut wires and is associated with the finite side length of the SRRs [24].

As we slowly increased the applied injection pressure, but kept it below  $\sim 296$  kPa, there were no changes in the device geometry. However, when the pressure exceeded  $\sim 296$  kPa, EGaIn flowed into the SRR gap channels. The resulting device structure, in which the SRRs switched over to being closed ring resonators (CRRs), is shown in Fig. 3(a). The measured

transmission spectrum, again with the incident THz radiation polarized perpendicular to the injection lines, is shown in Fig. 3(b). The double resonance associated with the SRRs has now abruptly changed to a single resonance within the spectral window. To validate this result, we also numerically simulated the transmission spectrum, shown in Fig. 3(c). Both spectra have a single resonance dip centered at 0.40 THz, although the experimentally measured resonance is shallower and broader. We attribute these differences to the same causes discussed above. In the case of CRRs, the LC response disappears and there is no coupled magnetic field. This explains the disappearance of the resonance centered at 0.17 THz. Similarly, the current distribution associated with the higher order resonance at 0.54 THz changes, causing it to disappear. In place of these two spectral features, there is now a resonance centered at 0.40 THz, which is the fundamental resonance mode of CRRs. As shown by the snapshot of the current distribution in Fig. 3(d), the current is distributed nearly evenly between the two side segments of equal length, parallel to the THz electric field and oscillating in-phase [25]. The resonance associated with CRRs is much broader than those for SRRs, which arises from the asymmetry of the ring shape along the electric field axis.

Up to this point, we have shown that the metamaterial can switch from SRRs to CRRs. While such switching has been demonstrated using a variety of techniques, the method used here can allow for further changes in the configuration, making this a potentially more flexible approach. To demonstrate this, we further increased the applied injection pressure. When the applied pressure was kept below  $\sim 386$  kPa, we found that there were no changes in the device geometry. However, when the pressure increased beyond  $\sim 386$  kPa, the narrow horizontal channel of width  $W_3$ , as well as the channels of width  $D_2$  and  $D_3$  filled with EGaIn (i.e. all channels in the device were filled). It should be noted that the latter two channels (of widths  $D_2$  and  $D_3$ ) were also filled because the critical pressure required to fill them was lower than  $\sim 386$  kPa. The resulting device configuration, which we refer to as an irregular CRR, is shown in Fig. 4(a).

In Fig. 4(b), we show the experimental transmission spectra, again with the THz electric field polarized perpendicular to the horizontal injection lines. The spectrum is characterized by a low frequency narrow linewidth resonance centered at 0.13 THz and a much broader linewidth resonance centered at 0.4 THz. In the numerically simulated response of this geometry, shown in Fig. 4(c), there is a low frequency narrow linewidth resonance centered at 0.13 THz. However, the higher frequency resonance is actually composed on two resonances: a resonance at 0.39 THz and a shallower resonance centered at 0.44 THz. The former resonance is similar to that shown in Fig. 3(c), though red-shifted by  $\sim 10$  GHz. In the experimental measurements, the linewidth of the resonance is sufficiently broad that the two separate resonances cannot be resolved.

The frequencies of each of these resonances can be understood by considering the relevant current distributions. In Fig. 4(d), we show a snapshot of the current distribution for an excitation frequency of 0.13 THz. The resonance is associated with the large rectangle-like closed rings that are formed by the right edge of adjacent unit cells and the upper and lower horizontal lines and is analogous to the response of CRRs. However, since the area of this composite structure is larger than the CRRs, the resonance is red-shifted. The resonance at 0.39 THz arises from the CRRs and is the same as seen in Fig. 3(d). In Fig. 4(e), we show a snapshot of the current distribution for an excitation frequency of 0.44 THz, which suggests that the resonance is associated with coupling between the CRR and the diagonal metallic line. In comparing Fig. 4(e) with Fig. 3(d), we find that the diagonal metallic line reduces the resonant dipole length to only the left half of the CRR. This reduced length increases the resonance frequency from 0.4 THz to 0.44 THz. This dipole resonance is the dominant part in Fig. 4(e). Because the dipole occurs only on one side of the structure (i.e. half of the left side of the CRR), the 0.44 THz resonance is shallower than the 0.4 THz resonance. In fact, for numerical simulations in which the diagonal line is removed, this high frequency contribution to the spectrum disappears.



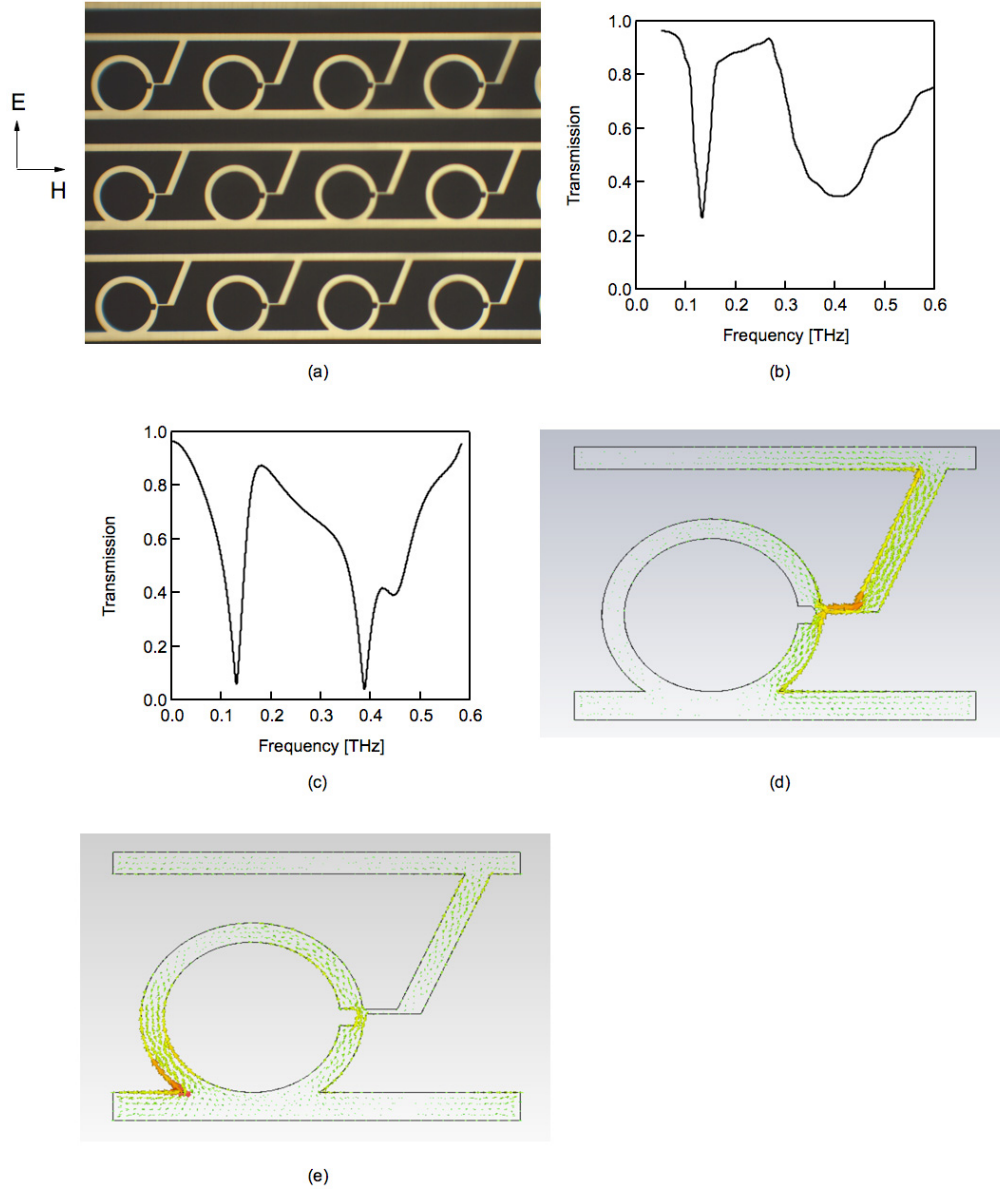


Fig. 4. (a) Photograph of a portion of the irregular ring array. (b) Measured transmission spectrum with the THz electric field polarized perpendicular to the horizontal injection lines. (c) Numerically simulated transmission spectrum under the same excitation scheme. (d) Snapshot of the numerically simulated current distribution using an excitation frequency of 0.13 THz. (e) Snapshot of the numerically simulated current distribution using an excitation frequency of 0.44 THz.

Filling the device required that the applied pressure exceed three different values for the critical pressure for three different geometries. In order to understand this behavior, we consider the relationship between the applied pressure and the channel dimensions. In a channel, the pressure,  $P$ , required to initiate flow is associated for a channel of width ( $W$ ) and height ( $H$ ) is given by

$$P = 2\gamma \cos(\theta) \left( \frac{1}{W} + \frac{1}{H} \right). \quad (2)$$



Here,  $\gamma$  is a parameter that is related to the interfacial force per unit length required for EGaIn to flow and  $\theta$  is the contact angle between EGaIn and PDMS ( $= 150^\circ$ ) [10]. Dickey et al. have previously found that  $\gamma = 0.63$  N/m in the microchannels that they used [10]. In Fig. 5, we plot the critical pressure as a function of the channel dimensions. In the case of the lower horizontal injection channel and the SRR, both filled simultaneously when the pressure exceeded  $\sim 255$  kPa, even though the two have slightly different dimension. Using Eq. (2), we fit a line to only the two higher pressure data points and find that the best fit value for  $\gamma$  is 0.58, in reasonable agreement to the value mentioned above. One possible reason for the slight difference in best-fit values for  $\gamma$  might arise from the actual dimensions for the SRR gap channel and the short horizontal channel of width  $W_2$ . In both cases, the channels lengths are only slightly larger than the corresponding channel widths. In earlier work, the channel length was more than tens times its width, which may affect the required pressure [10]. In addition, the rectangular cross-section channels may deform slightly under pressure and, thus, correspond to different dimensions than used in Eq. (2). Finally, it should be noted that Eq. (2) is only an approximation, since it is very difficult to analyze the interfacial curvature in a rectangular shaped channel.

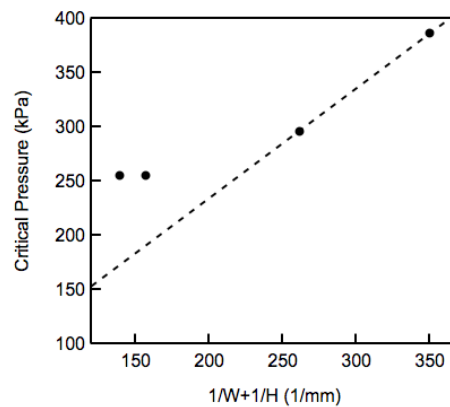


Fig. 5. The critical applied pressure required for filling EGaIn for each channel segment as a function of the sum of the inverse height ( $H$ ) and width ( $W$ ). The dashed line is a best-fit to only the two higher pressure data points. The slope of the best-fit line to the data for EGaIn is 1.01 N/m.

Based on the dimensions of the channels and the best fit value for  $\gamma$ , we would expect that the critical pressure required for EGaIn to flow into the lower injection channels of width  $D_1$  to be  $\sim 140$  kPa and the critical pressure required to fill the SRR channels of width  $W_1$  to be  $\sim 159$  kPa. The need for a much larger applied pressure to fill these two channels can be attributed to several issues. First, the large difference between the dimensions of the inlet reservoir and the injection channels may cause the required injection pressure to deviate from Eq. (2). Second, the thickness of the PDMS layer in the device described here was much thinner than was used in [10]. The increased gas permeability would lead to a significant increase in the required critical pressure. Third, the distance between the rings and the outlet affects the required pressure. If the rings were too close to the outlet, EGaIn would simply flow out of the injection channel without ever entering the rings. Given that the critical pressures for filling the injection channels and the SRR channels are very close, it is difficult to fill only the injection channels, without having any leakage into the SRRs. In fact, we did not observe two separate critical pressures for the two different channels.

In order to demonstrate full reconfigurability, there needs to be a final step that allows the device to be reset to its original configuration. As noted earlier, an oxide surface layer forms on the liquid metal stabilizing its configuration. In the absence of this oxide, EGaIn has a viscosity that is twice that of water and a surface tension that is similar to that of Hg. Since PDMS is gas permeable, the oxide layer can be dissolved using acids. Therefore, when the

entire device is exposed to hydrochloric acid (HCl), in the presence of light mechanical pressure, the oxide layer surrounding the EGaln metal within the device can be quickly dissolved, at which point the EGaln retracts out of the microchannels and returns to either the inlet or the outlet. In Fig. 6(a), we show an image of the device after it has been exposed to HCl for 1 minute. In Fig. 6(b), we show the corresponding transmission spectrum. It is clear that although several small remnants of liquid metal remain in some of the channels, they have no impact on the transmission properties of the reset device.

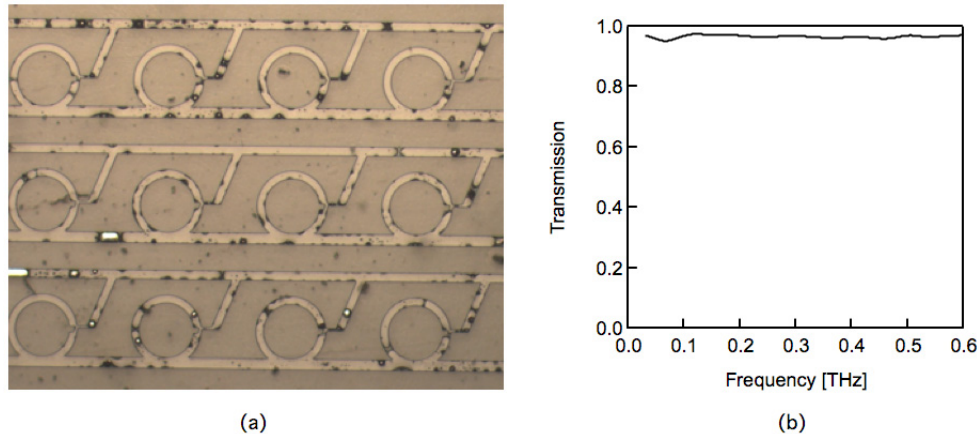


Fig. 6. Properties of the reset device. (a) Photograph of a portion of the reset device (all of the EGaln was returned to either the inlet or the outlet). The two short white line segments correspond to EGaln that remained in the upper and lower horizontal channels. The different contrast in the image, as compared the earlier figures, was used to more clearly show the channel properties after resetting the device. (b) The corresponding transmission spectrum.

#### 4. Conclusion

In summary, we have demonstrated a reconfigurable metamaterial device that utilizes liquid metal, EGaln, as its metallic element. The device utilizes conventional microfluidic technology, where microchannels in the form of ring resonators are created in a PDMS mold. By carefully designing the dimensions of the microchannels, we can require different critical pressures for different segments of the device. Therefore, only specific sections of the device are filled with EGaln when the corresponding critical pressure is exceeded. This allows for a device geometry that can change abruptly from one configuration to another, enabling dramatic changes in the corresponding transmission properties. Since it is the metallic elements that are changed, the number of possible configuration changes is limited only by the available pressure differences that can be set. Thus, such a device is not limited to the conventional two state configuration. In addition, because the liquid metal flow conditions are irreversible, in a general sense, the transmission spectra records the pressure applied to the liquid metals, providing a means for sensing and recording the external pressure through THz electromagnetic fields. Such a capability may be useful in structures that incorporate not only liquid metals, but also other liquids to create devices that combine plasmonics with more conventional microfluidic capabilities. Finally, although we only describe only one specific metamaterial geometry, the approach can be applied to a broad range of THz device technologies.

#### Acknowledgments

This work was supported by the NSF MRSEC program at the University of Utah under grant # DMR 1121252.